Electric and Photovoltaic Behavior of a Few-Layer α-$MoTe_2$/MoS_2 Dichalcogenide Heterojunction

*Atiye Pezeshki, Seyed Hossein Hosseini Shokouh, Tavakol Nazari, Kyunghwan Oh, and Seongil Im**

Transition-metal dichalcogenides (TMDs) are two-dimensional (2D) nanomaterials with the common formula MX_2, where M is a transition metal from group IV–VII (M = Mo, W, Nb, Re, and so on), while X is a chalcogen (X = S, Se, Te). In general, M atoms are sandwiched between X atoms to form a single layer, and each layer is stacked together by van der Waals forces,[1] which make 2D TMDs easily cleaved by scotch tape[2,3] or other similar techniques.[4–8] Among TMD families with ultrathin layers, molybdenum disulfide (MoS_2) and tungsten diselenide (WSe_2) are well-known semiconductors with bandgaps of more than 1 eV; their bandgap increases to ca. 1.6–1.8 eV for monolayers and band properties changes from indirect to direct type.[9–12] A recently produced 2D material, molybdenum ditelluride, (α-$MoTe_2$) has also attracted attention due to its optical and electrical properties.[3,13,14] Monolayer α-$MoTe_2$ exhibits a direct optical bandgap of 1.10 eV,[12,13] while its bulk form becomes an indirect semiconductor with a bandgap of 0.88 eV.[12,15] α–$MoTe_2$ shows structural and electronic phase transitions. The structural phase transition from hexagonal phase to monoclinic distorted octahedral or 1T′ phase is reversible at a high temperature.[16]

Few-layered α-$MoTe_2$ field-effect transistors (FETs) show ambipolar or p-type conduction,[3,16–19] with a broad range of mobility such as ca. 0.2–40 $cm^2\ V^{-1}\ s^{-1}$. However, a $MoTe_2$-based homo- or heterojunction p–n diode was not yet reported, although the p–n diode is a basic building block for electronics and optoelectronics. Forming two different types of conduction in the same nanoflake might not be easy, since it often needs chemical or gate-induced electrical doping which is unstable or makes device structures complicated.[20–23] So, heterojunction p–n diode studies have always been limited to n-MoS_2/p-Si bulk,[24,25] n-MoS_2/p-WSe_2,[26–31] and n-MoS_2/p-BP (black phosphorous) systems.[32] Among the reported heterojunction p–n diodes, the n-MoS_2/p-Si diode does not represent all 2D p–n junction cases and the n-MoS_2/p-BP diode does not appear to have high performance without gate support from SiO_2/p-Si substrate. So, the n-MoS_2/p-WSe_2 system appears to be the best candidate performance-wise but it also often needs the same gate support or dipole-induced electrostatic hole doping for a few layer p-WSe_2 layer, which is not very conductive due to its low hole-carrier density.

Herein, we attempt to fabricate a p–n diode van der Waals heterojunction by direct imprinting,[4] by transferring p-type α-$MoTe_2$ onto an n-type MoS_2 nanoflake; this is inspired by the achievement of the Mo-based dichalcogen 2D p–n diode in this way; p-type α-$MoTe_2$ should be more conductive than p-type WSe_2 because its bandgap is smaller than that of WSe_2. Such a Mo-based p–n diode should be a model device for a chemical-vapor-deposited (CVD) $MoTe_2$/MoS_2 junction, which would simply be formed by changing the Te source from S on the oxidized Mo layer without changing the transition metal[33,34] (unlike the WSe_2/MoS_2 system). Pt electrode appeared to be very good for ohmic contact with α-$MoTe_2$ even without thermal annealing, and also secured a few-layer α-$MoTe_2$ as a strong p-type semiconductor. Our few-layered α-$MoTe_2$/MoS_2 p–n diode demonstrates low voltage operation at 5 V and high reasonable ON/OFF current ratio of about $10^3 - 4 \times 10^3$ (about 4×10^3 on SiO_2/Si and 10^3 on glass substrate) along with good ideality factors of around 1.06–1.34. Kilohertz fast dynamic rectification was achieved in the dark while dynamic photovoltaic switching was also exhibited under red, green, and blue light-emitting diodes (LEDs), and 800-nm infrared laser. The photoresponse time appears to be at longest 25 ms, as measured from the about 1–3 Hz photoswitching dynamics; this is a temporal way to harvest energy because visible photons can dynamically switch 2D photovoltaic devices at zero-volt state. Moreover, such a dynamic photovoltaic switching has rarely been reported in application, although this type of self-powered dynamic voltage generation can have a variety of applications as UV- and visible-light detection, biological and chemical study in a wireless healthcare platform, powerless communications, and so on.[35] Our 2D p–n diode is quite promising for nano- and optoelectronics.

A schematic 3D view of the α-$MoTe_2$/MoS_2 nanoflake p–n diode on glass or 285 nm-SiO_2/Si substrate is shown in **Figure 1**a, where Au/Ti and Pt contacts are separately used for n-type MoS_2 and p-type $MoTe_2$. (Fabrication details are explained in the Experimental Section section.) We use Pt for α-$MoTe_2$, because its work function (ca. 5.2 eV) should be deeper than the Fermi level or valence band maximum (ca. 4.7–4.99 eV based on theoretical calculation[36]) of p-type $MoTe_2$. According to Figure S1 (Supporting Information); good ohmic contact behavior occurs from the p-channel $MoTe_2$ FET with a

A. Pezeshki, S. H. H. Shokouh, T. Nazari, Prof. K. Oh, Prof. S. Im
Institute of Physics and Applied Physics
Yonsei University
50 Yonsei-ro, Seodaemun-gu, Seoul 120–749, South Korea
E-mail: semicon@yonsei.ac.kr

DOI: 10.1002/adma.201504090

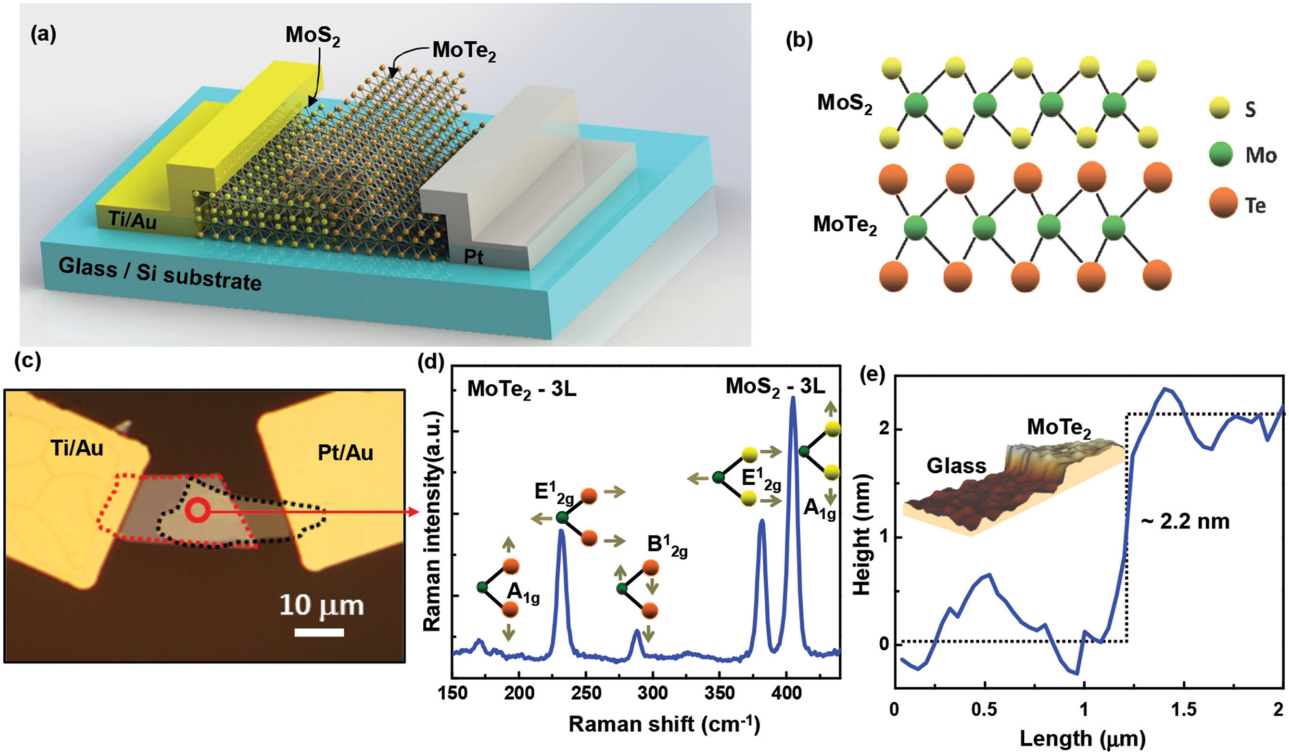

Figure 1. Schematic 3D view of (a) our Mo-based p–n diode comprised of n-MoS_2 and p-$MoTe_2$ nanoflakes on glass. b) Hexagonal structures of MoS_2 and $MoTe_2$ nanoflakes. The yellow, green, and orange balls show sulfur, molybdenum and telluride atoms, respectively. c) Optical microscopy (OM) images of a p–n diode on a glass substrate. (Black and red dashed lines indicate $MoTe_2$ and MoS_2 nanoflake, respectively). Direct imprinting was used to realize the $MoS_2/MoTe_2$ heterojunction p–n diode. d) Raman spectra obtained from both $MoTe_2$ and MoS_2 flakes at once, with an estimated thickness of 3L for both $MoTe_2$ and MoS_2 nanoflakes. (See arrow; the excitation wavelength was 532 nm.) e) AFM line profile shows the thickness of 3L-thin α–$MoTe_2$ flake on glass (ca. 2.2 nm).

Pt source-drain electrode. Good ohmic contact between Pt and α-$MoTe_2$ was obtained even without any thermal annealing, while the MoS_2 channel usually required postannealing for better contact with Ti/Au. Optical microscope images of the two p–n diodes on glass and 285 nm-SiO_2/Si substrates are respectively shown in Figure 1c and Figure S2a (Supporting Information). The layer thickness or numbers of α-$MoTe_2$ and MoS_2 were determined by using micro-Raman spectroscopy (Figure 1d) and confirmed by atomic force microscopy (AFM; Figure 1e and Figure S2c, Supporting Information). Raman spectroscopy was used to probe both the p and n regions (arrows indicate these in Figure 1c and Figure S2b, Supporting Information) all at once by using 532 nm excitation to distinguish the two different 2D materials for the p and n regions. According to the Raman results in Figure 1d and Figure S2b (Supporting Information), in-plane E^1_{2g} and out-of-plane A_{1g} vibration modes in MoS_2 are much larger in wavenumber than those of $MoTe_2$. $MoTe_2$ layers even show a B^1_{2g} vibration peak. MoS_2 and α-$MoTe_2$ layers should have the same hexagonal structure but different bond length, as shown in the schematic monolayers of Figure 1b; the Mo–Te bond length is longer than that of Mo–S so causes smaller vibration frequencies in the $MoTe_2$ system than in the MoS_2 one. Based on their peak position/intensity information in the Raman spectra[12–14,37] and AFM results, the layer numbers (or thickness) are estimated to be about 3L for both $MoTe_2$ and MoS_2 on glass while the other sets on SiO_2/Si substrate are around 4L for both p and n layers. We attempted photoluminescence (PL) measurements as well to distinguish the two different 2D materials, by using the same 532 nm laser probing on the same spot as for Raman spectroscopy. As a result (seen in Figure S2d and S2e, Supporting Information), our PL spectra displayed two different emission regions at about 790 nm (1.56 eV) and 1150 nm (1.08 eV), which nicely resolves the two materials.

Current-voltage (I–V) curves of our p–n diodes on SiO_2/Si and glass are shown in **Figure 2**a, where the ON current of the p–n diode on SiO_2 is a few times higher than that of the other diode on glass; this is expected because the p–n junction area of the diode on SiO_2 was initially larger than that on glass (see Figure 1c and Figure S2a, Supporting Information). Ideality factors of our diodes are in the range from 1.06 (on glass) to 1.34 (on SiO_2) and their ON/OFF ratios are in the range of about $10^3 - 4 \times 10^3$ under ±5 V operating conditions. Since both devices show quite similar behavior, we chose the p–n diode on the glass substrate for more extended study while the device performances of the SiO_2-supported device are given in Figure S3 (Supporting Information). Inset of Figure S3 (Supporting Information) shows the circuit symbol of the p–n diode. Figure 2b shows applied input voltage (V_{IN}) vs. output voltage (V_{OUT}) plots respectively obtained from the inset circuit with three different external resistors of 1, 10, and 100 MΩ Under a reverse bias (positive V_{IN} applied to n-MoS_2), the p–n

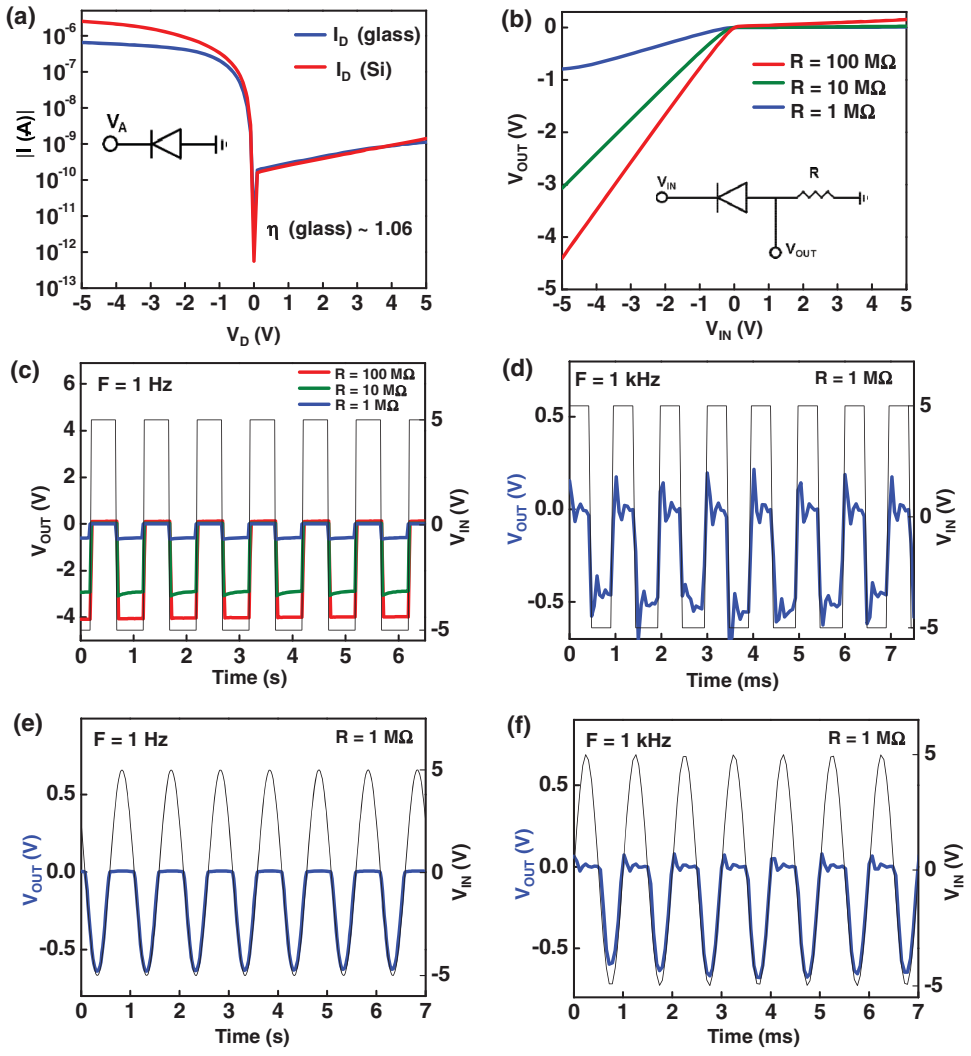

Figure 2. a) Current–voltage (*I–V*) curves of p–n diode on glass and SiO_2/p+-Si (285 nm) substrates in a logarithmic scale with circuit configuration (inset). b) V_{IN}–V_{OUT} curves of our p–n diode circuit (inset) on glass at different external resistances (*R*) of 1, 10, 100 MΩ, was obtained by sweeping V_{IN} from –5 V to 5 V. Rectified dynamic output voltage was obtained by applying an AC square wave of V_{IN} = ±5 V at (c) 1 Hz for R = 1, 10, and 100 MΩ, (d) 1 kHz for *R* = 1 MΩ. Such rectification dynamics were also realized by applying AC sine waves of V_{IN} = ±5 V for *R* = 1 MΩ at (e) 1 Hz and (f) 1 kHz.

adiode should be so highly resistive that the circuit may achieve a rectified output signal of almost 0 V. Alternating the V_{IN} with ± 5 V square pulse at 1 Hz and 1 kHz resulted in dynamically rectified V_{OUT} signals, as shown in Figure 2c and d, respectively. In such dynamics, we used 1 MΩ as an external resistor and found that at 1 Hz the V_{OUT} signal had the same value as in Figure 2b (–0.7 V under –5 V input). However, the value of V_{OUT} fluctuates from –0.7 to –0.5 V at 1 kHz, probably due to some noise from contact, while no delay is observed. Similar rectification dynamics were observed by applying sinusoidal V_{IN} at 1 Hz (Figure 2e) and 1 kHz (Figure 2f).

Figure 3a,b show the photoinduced *I–V* curves of our α-$MoTe_2$/MoS_2 p–n diode, on logarithmic and linear scales. Red (620 nm, 1.3 mW), green (520 nm, 2.3 mW), blue (470 nm, 3 mW) light-emitting diodes (LED), and infrared (IR, 800 nm, 120 mW) laser were used to illuminate our device from an identical distance (2 mm away). Because of the different optical power density of the LEDs and laser beams, different open circuit voltage (V_{OC}) and short circuit current (I_{SC}) values are observed in Figure 3c and d, as magnified from the circled area of the *I–V* curves in Figure 3b. The V_{OC} values are only about –0.06 to –0.11 V for visible photons but appear to be as large as –0.32 V for 800 nm IR. Similarly, the I_{SC} value ranges from 2–7 nA for visible photons, while an IR laser produces about 150 nA. This result is unsurprising because the laser IR intensity should be around 60 times higher than that of visible photons in the present experiment. However, for more detailed analysis based on the photoinduced *I–V* curves of Figure 3c and d, we also estimated a zero volt spectral responsivity of our p–n diode, to be plotted in Figure 3e. According to the plot, blue photons show a responsivity value of about 322 mA W^{-1} and this decreases as the photon energy decreases (with a lowest value of 37 mA W^{-1} for 800 nm IR; see Table S1, Supporting Information). Such responsivity behavior and values are comparable to those of other 2D devices (also see Table S2, Supporting Information).[26] The responsivity plot of the 2D heterojunction

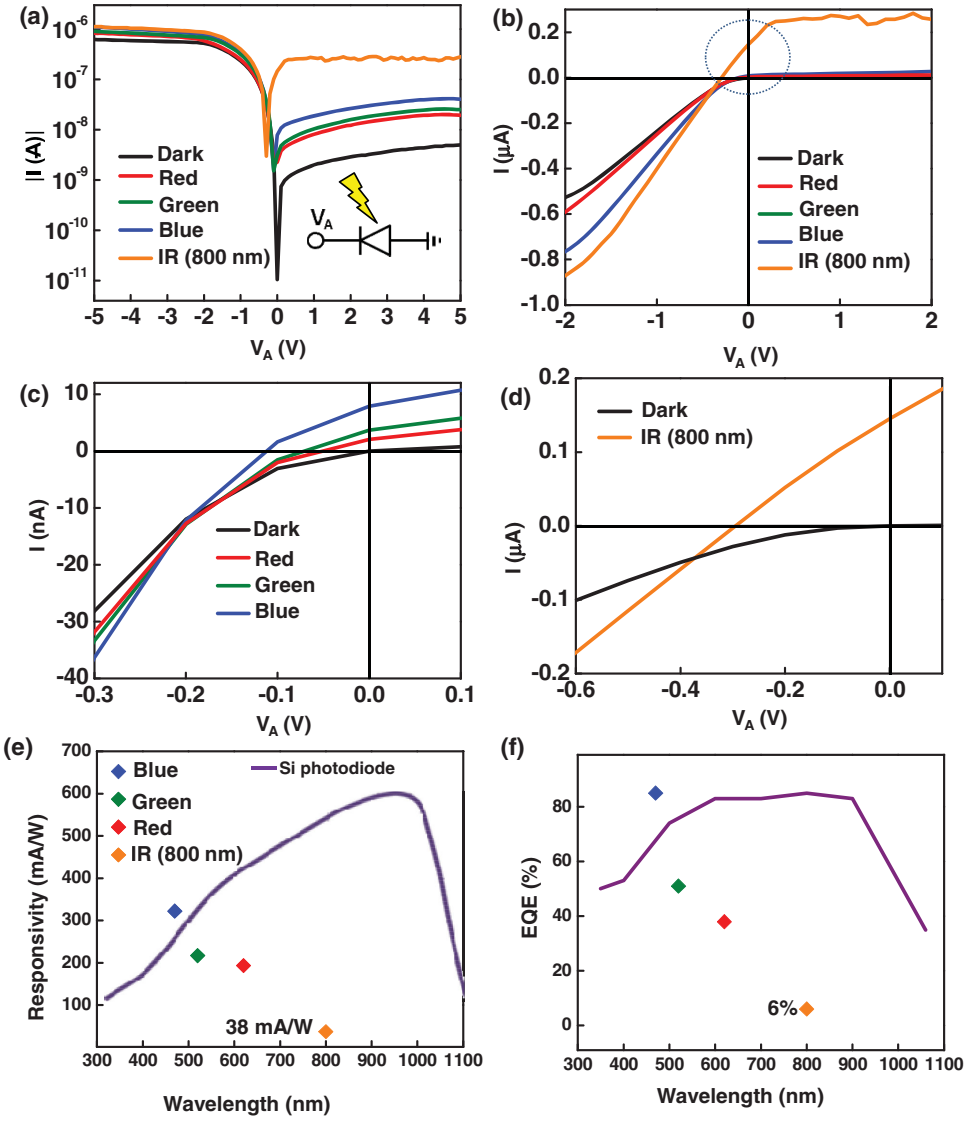

Figure 3. Photoinduced *I–V* curves of heterojunction p–n diode on glass under dark, red, green, blue LED, and IR (800 nm) illuminations (a) on a logarithmic scale along with circuit configuration (inset) and (b) on a linear scale. We magnified the *I–V* curves (blue dashed line) under (c) RGB LEDs and (d) IR laser (800 nm) illuminations on the linear scale to provide more precise V_{OC} and I_{SC} values. e) Photoresponse characteristics of our p–n junction diode under RGB LEDs and IR (800 nm) laser, obtained at zero volt. For comparison, the responsivity of a typical Si photodiode is added. f) External quantum efficiency (EQE) plots of our p–n diode and a typical Si photodiode, as a function of light wavelength.

diode is quite different to that of a bulk Si p–n diode,[38] where irradiation in the near IR (ca. 900 nm) results in the maximum responsivity with the Si bandgap of 1.12 eV (ca. 1100 nm); the responsivity decreases with the photon energy as shown in the solid line of Figure 3e. External quantum efficiency (EQE, %) plots of 2D and bulk Si p–n diodes exactly follow their respective responsivity behavior (Figure 3f). Such behavior may be typical of a 2D p–n diode,[26] whose thickness is too thin for depth-penetration effects of over-bandgap photons, unlike in the bulk Si diode case. The responsivity of the bulk Si diode is influenced by both penetration depth and energy of incoming photons, so for most visible and near-IR photons the conventional Si p–n diode should be better than our prototype 2D diode because such low energy photons penetrate into the Si by more than a few micrometers, to generate electrons and holes. However, the penetration depth in Si decreases with the photon energy; more energetic photons such as from blue and ultraviolet (UV) lights will have shallower penetration depths of a few tens of nanometers, along with lower responsivity (the p–n junction is normally located at a depth from the p-Si surface, so will not be excited by high-energy photons).[39] This situation means that for high-energy photons our thin 2D p–n diode may respond more efficiently than does the Si diode, as indeed shown in Figure 3e and 3f. Our 2D p–n diodes are thus promising for more energetic photons than is the case for near IR (which is barely higher than the bandgap energies of 3L MoS_2 and $MoTe_2$: ca. 1.5 and 1 eV), for photovoltaic applications.

The photovoltaic effects observed with photoinduced *I–V* characteristics (Figure 3a–d) are directly applied to dynamic photovoltaic switching (at 1 Hz) which would be more practical

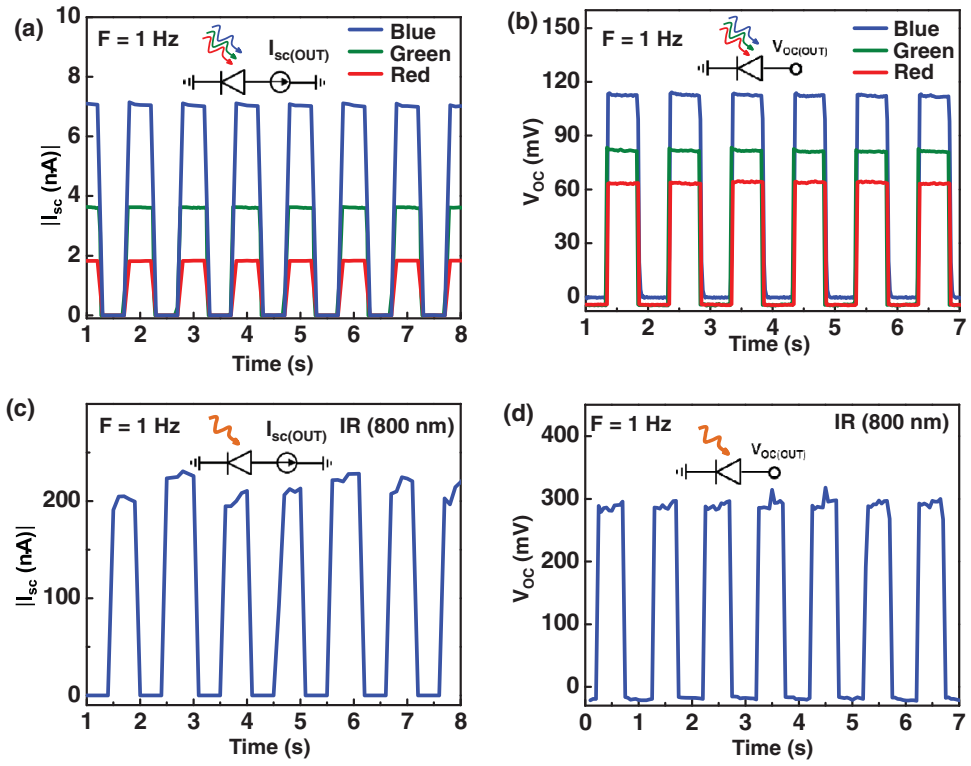

Figure 4. Time domain of (a) short-circuit current (I_{SC}) and (b) open-circuit voltage (V_{OC}) values obtained from our single p–n diode under periodic 1-Hz RBG LEDs illuminations. (Each inset shows schematic diode circuits.) Time domain of (c) I_{SC} and (d) V_{OC} values were measured under periodic 1 Hz IR (800 nm) laser illumination for our Mo-based p–n diode.

and enable us to harvest energy, as shown in **Figure 4**a–d. The photovoltaic switching is used to measure values of I_{SC} and V_{OC} (as I_{OUT} and V_{OUT}) without an electrical power supply, as seen in the inset circuits of Figure 4a and b. According to I_{SC} and V_{OC}, the I_{SC} (I_{OUT}) values obtained from visible lights are limited to 2, 4, and 7 nA while V_{OC} appears to be 60, 80, and 110 mV. The photoresponse time appears to be about 25 ms, as measured at 3 Hz under a red laser (630 nm, 4.8 mW, Figure S4, Supporting Information). These results are consistent with those shown in Figure 3c. Dynamic I_{SC} and V_{OC} values at 800-nm IR irradiation also follow the results from Figure 3d, displaying maximum current and voltage of about 200 nA and 0.3 V, respectively.

The photoinduced voltages from our 2D p–n (or n–p) junction diode are explained in the schematic band diagrams of **Figure 5**a–c. Figure 5a shows an energy-band diagram of individual MoS_2 and α-$MoTe_2$ (n–p) systems before heterojunction formation. (In the figure n–p junction drawings are shown for the viewer's convenience, following the schematic device cross-section in Figure 5d. We initially transferred MoS_2 onto glass, and then the $MoTe_2$ flake was transferred onto MoS_2). The energy levels in Figure 5a are based on a previous report which summarizes the theoretical calculation values of conduction and valence band edge on various TMD layers.[36] According to Figure 5a and the report, the calculated difference between the conduction band minimum of MoS_2 and valence band maximum of α-$MoTe_2$ would be about 0.35 eV (again, this value is based on literature[36] and the actual value could be higher). If charge transfer takes place between p–type α-$MoTe_2$ and n-type MoS_2 after heterojunction formation (despite the van der Waals junction gap (ca. 0.3 nm in general)), a schematic hetero n–p junction band diagram is expected to be like that in Figure 5b. However, more details regarding the potential drops in 3L-thick n, 3L-thick p, and 3-Å-thick van der Waals junction gap regions could be described, so we show those in Figure S5 (Supporting Information) for zero, forward, and reverse bias conditions. When energetic photons fall onto the diode, as seen in the diagram and device cross-section scheme of Figure 5c and d, the band diagram changes from that in Figure 5b to that in Figure 5c, because the photoexcited holes and electrons move to the p- and n-side, respectively. Then, photoinduced voltage (V_{photo}) is generated, but probably has its theoretical maximum at about 0.35 V, which arises from the difference between the conduction band minimum of MoS_2 and the valence band maximum of α-$MoTe_2$. This estimate is based on an organic heterojunction p–n diode solar cell, where the situation may be similar to our van der Waals heterojunction diode.[40] In consideration of the lateral (charge-neutral) region resistance (see Figure 5d) and exciton binding energy of 2D semiconductors, measured V_{OC} should not be higher than the theoretical maximum value (0.35 V) regardless of the 120 mW high optical power of the 800-nm IR laser, which thus results in about 0.3 V as V_{OC} in Figure 3d and Figure 4d. 3 mW low-power blue visible photons produce limited V_{OC} (V_{OUT}) values that are lower than 0.11 V because of two issues: low light intensity, which may not be enough to make a maximum V_{OC} and a serious potential drop in large lateral resistance which could be reduced by high-intensity photoexcitation (as is the case for the IR laser). We thus believe that V_{OC} output would be smaller than 0.35 V.

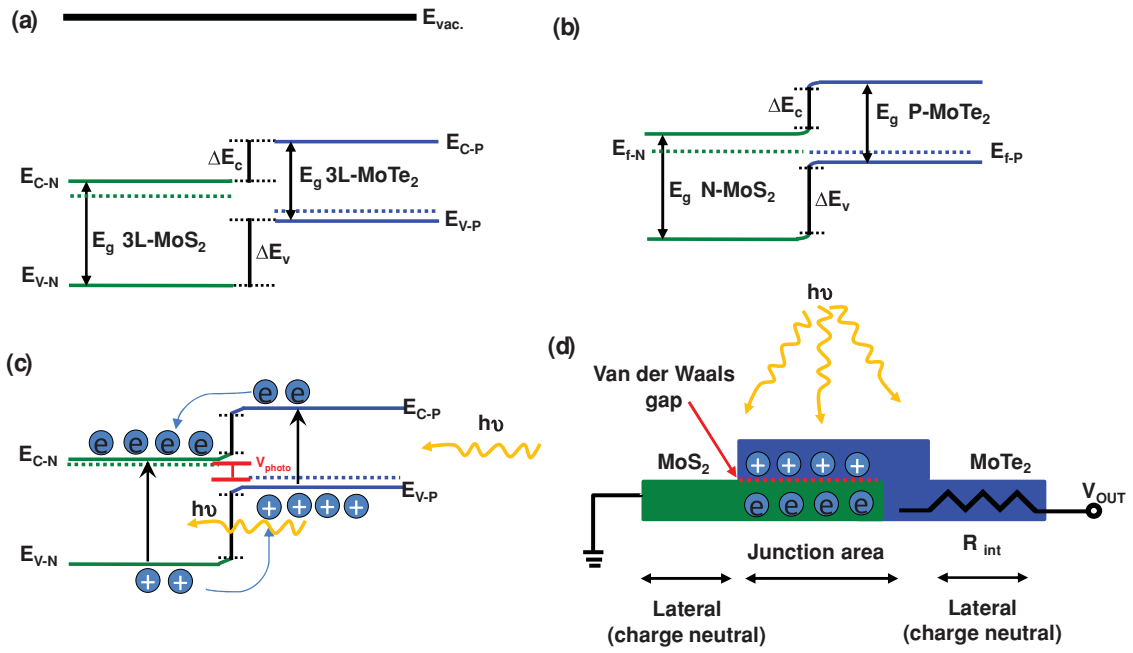

Figure 5. a) Energy-band diagram of 3L-MoS_2 and 3L-$MoTe_2$ before realizing the Mo-based heterojunction, where E_C and E_V are conduction-band edge and valence-band edge, E_F is Fermi energy level, ΔE_C means conduction-band offset between MoS_2 and $MoTe_2$, ΔE_V is valence-band offset between MoS_2 and $MoTe_2$, E_g is bandgap energy, and E_{vac} is vacuum energy level. Energy-band diagrams at the interface between MoS_2 and $MoTe_2$ of our p–n junction diode (b) at equilibrium, (c) and under illumination. V_{photo} refers to the photoinduced voltage and its maximum would be the difference between $E_{C\text{-}N}$ and $E_{V\text{-}P}$. d) Cross-section schematic of our Mo-based p–n heterojunction diode, which actually contains internal resistance resulting from the charge neutral (lateral) region.

In summary, we have fabricated van der Waals heterojunction p–n diodes with two different TMD nanoflakes of p-type α-$MoTe_2$ and n-type MoS_2, to achieve Mo-based dichalcogen 2D p–n diode on glass and SiO_2/Si substrates. A Pt electrode appeared to give good ohmic contact with p-type α-$MoTe_2$. Our few-layered α-$MoTe_2$/MoS_2 p–n diode demonstrates low-voltage operation at 5 V and a high ON/OFF current ratio of about $10^3 - 4 \times 10^3$, along with ideality factors of around 1.06–1.34. Dynamic rectification was demonstrated at a high frequency of 1 kHz on glass. Photovoltaic effects were also characterized by means of photoinduced *I–V* curves and band diagrams, measured using 800-nm-IR, red, green, and blue illuminations. The highest responsivity value (322 mA W^{-1}) and EQE (85%) were achieved under zero-bias from blue photons. A maximum open-circuit voltage of about 0.3 V was confirmed by dynamic photovoltaic switching of high-power 800-nm IR light. We conclude that our few-layered α-$MoTe_2$/MoS_2 p–n diode is promising as a Mo-based nanosystem to provide high-frequency rectification and photovoltaic-switching capabilities for future nanoelectronics.

Experimental Section

Device Fabrication: p-$MoTe_2$ and n-MoS_2 nanoflakes were used to fabricate a van der Waals heterojunction p–n diode on glass and 285 nm-thick SiO_2/p^+-Si substrates. The substrates were ultrasonically cleaned in acetone, methyl alcohol, and deionized water and then dried by N_2 flow. Bulk MoS_2 and $MoTe_2$ crystals (commercially available; α-$MoTe_2$: HQ graphene and MoS_2: SPI supplies) were exfoliated by using transparent polydimethylsiloxane (PDMS), so we searched for appropriate few-layer MoS_2 or $MoTe_2$ flakes by using the optical microscope. The optical transparency of flakes is different with back illumination, depending on the layer thickness. Then, we transferred thin MoS_2 and $MoTe_2$ nanoflake, by the direct imprinting technique.[4] Therefore, the $MoTe_2$ flakes could be aligned on few-layer MoS_2. So, we had a heterojunction area of both n-type and p-type Mo-based semiconductors on glass or 285 nm-thick SiO_2/p^+-Si substrate. The electrodes were patterned by using conventional photolithography.[41] Then, to form a heterojunction p–n diode, 25 nm-thick Ti and 50 nm-thick Au layers (Au/Ti) were deposited as ohmic contacts for the MoS_2 nanoflake and 25 nm-thick Pt and 50 nm-thick Au layers (Au/Pt) for the $MoTe_2$ nanoflake, by using a DC magnetron sputtering system as shown in the OM images of Figure 1c, and Figure S2a (Supporting Information). For the lift-off process, acetone and lift-off layer (LOL) remover were used.

Electrical and Photovoltaic Measurements: Atomic force microscopy (AFM) equipment (XE-Bio, park systems) was used to measure the flake thickness and Raman spectroscopy was performed by using a Raman spectrometer (LabRam, Horriba Jovin Yvon). All device characterizations were performed in the dark at room temperature by using a semiconductor parameter analyzer (HP4155C, Agilent Technologies), and a function generator (AFG 310, Tektronix) was used for dynamic measurements. The photocurrent density is defined as $J_{ph} = J_{Illumination} - J_{Dark}$, where $J_{Illumination}$ and J_{Dark} are respective current densities (J) without and with illumination; $J = I/$(p–n junction area). The (photo)responsivity defined as $J_{ph}/P_{laser/LED}$, where $P_{laser/LED}$ is the incident optical power density of the laser or LED, defined as optical power/illuminating area.[29] The external quantum efficiency (EQE) is calculated by EQE = $(J_{SC}/P_{Laser})(hc/e\lambda)$, where J_{SC} is short circuit current density, h is the Planck constant, e is the electron charge, c is the velocity of light, and λ is the wavelength of the incident light. Laser power supply (CL-2000 diode pumped crystal) was used for the 800-nm IR illumination (120 mW, 3.73 W cm^{-2}). Red (1.3 mW, ~6.6 mW cm^{-2}),

green (2.3 mW, ca. 12 mW cm^{-2}), and blue (3 mW, ca. 15 mW cm^{-2}) LEDs were also used for photovoltaic effect characterizations of our 2D p–n diodes. Illuminated areas were 3.2×10^{-2} cm^2 for the IR laser and 1.96×10^{-1} cm^2 for RGB LEDs. The heterojunction area of our p–n diode on glass is 1.42×10^{-6} cm^2.

Supporting Information

Supporting Information is available from the Wiley Online Library or from the author.

Acknowledgements

A. P. and S. H. H. S. equally contributed to this work. The authors acknowledge financial support from NRF (NRL program: Grant No. 2014R1A2A1A01004815), Nano-Materials Technology Development Program (Grant No. 2012M3A7B4034985), and Brain Korea 21 plus Program, the Yonsei University (Future-leading Research Initiative of 2014: Grant No. 2014-22-0168).

Received: August 21, 2015
Revised: January 16, 2016
Published online: February 29, 2016

[1] S. Kim, A. Konar, W.-S. Hwang, J. H. Lee, J. Lee, J. Yang, C. Jung, H. Kim, J.-B. Yoo, J.-Y. Choi, Y. W. Jin, S. Y. Lee, D. Jena, W. Choi, K. Kim, *Nat. Commun.* **2012**, *3*, 1011.
[2] J. N. Coleman, M. Lotya, A. O'Neill, S. D. Bergin, P. J. King, U. Khan, K. Young, A. Gaucher, S. De, R. J. Smith, I. V. Shvets, S. K. Arora, G. Stanton, H.-Y. Kim, K. Lee, G. T. Kim, G. S. Duesberg, T. Hallam, J. J. Boland, J. J. Wang, J. F. Donegan, J. C. Grunlan, G. Moriarty, A. Shmeliov, R. J. Nicholls, J. M. Perkins, E. M. Grieveson, K. Theuwissen, D. W. McComb, P. D. Nellist, V. Nicolosi, *Science* **2011**, *331*, 568.
[3] S. Fathipour, N. Ma, W. Hwang, V. Protasenko, S. Vishwanath, H. G. Xing, H. Xu, D. Jena, J. Appenzeller, A. Seabaugh, *Appl. Phys. Lett.* **2014**, *105*, 192101.
[4] K. Choi, Y. T. Lee, S.-W. Min, H. S. Lee, T. Nam, H. Kim, S. Im, *J. Mater. Chem. C* **2013**, *1*, 7803.
[5] S. H. Hosseini Shokouh, A. Pezeshki, S. R. A. Raza, K. Choi, S.-W. Min, P. J. Jeon, H. S. Lee, S. Im, *ACS Nano* **2014**, *8*, 5174.
[6] S. H. Hosseini Shokouh, A. Pezeshki, S. R. Ali Raza, H. S. Lee, S. W. Min, P. J. Jeon, J. M. Shin, S. Im, *Adv. Mater.* **2015**, *27*, 150.
[7] A. Pezeshki, S. H. Hosseini Shokouh, S. R. A. Raza, J. S. Kim, S.-W. Min, I. Shackery, S. C. Jun, S. Im, *J. Mater. Chem. C* **2014**, *2*, 8023.
[8] Y. T. Lee, K. Choi, H. S. Lee, S.-W. Min, P. J. Jeon, D. K. Hwang, H. J. Choi, S. Im, *Small* **2014**, *10*, 2356.
[9] B. Radisavljevic, A. Radenovic, J. Brivio, V. Giacometti, A. Kis, *Nat. Nanotechnol.* **2011**, *6*, 147.
[10] A. Splendiani, L. Sun, Y. Zhang, T. Li, J. Kim, C.-Y. Chim, G. Galli, F. Wang, *Nano Lett.* **2010**, *10*, 1271.
[11] H. S. Lee, S.-W. Min, Y.-G. Chang, M. K. Park, T. Nam, H. Kim, J. H. Kim, S. Ryu, S. Im, *Nano Lett.* **2012**, *12*, 3695.
[12] I. G. Lezama, A. Arora, A. Ubaldini, C. Barreteau, E. Giannini, M. Potemski, A. F. Morpurgo, *Nano Lett.* **2015**, *15*, 2336.
[13] C. Ruppert, O. B. Aslan, T. F. Heinz, *Nano Lett.* **2014**, *14*, 6231.
[14] M. Yamamoto, S. T. Wang, M. Ni, Y.-F. Lin, S.-L. Li, S. Aikawa, W.-B. Jian, K. Ueno, K. Wakabayashi, K. Tsukagoshi, *ACS Nano* **2014**, *8*, 3895.
[15] I. G. Lezama, A. Ubaldini, M. Longobardi, E. Giannini, C. Renner, A. B. Kuzmenko, A. F. Morpurgo, *2D Mater.* **2014**, *1*, 021002.
[16] D. H. Keum, S. Cho, J. H. Kim, D.-H. Choe, H.-J. Sung, M. Kan, H. Kang, J.-Y. Hwang, S. W. Kim, H. Yang, K. J. Chang, Y. H. Lee, *Nat. Phys.* **2015**, *11*, 482.
[17] Y. F. Lin, Y. Xu, S. T. Wang, S. L. Li, M. Yamamoto, A. Aparecido-Ferreira, W. Li, H. Sun, S. Nakaharai, W. B. Jian, K. Ueno, K. Tsukagoshi, *Adv. Mater.* **2014**, *26*, 3263.
[18] S. Nakaharai, M. Yamamoto, K. Ueno, Y.-F. Lin, S. Li, K. Tsukagoshi, *ACS Nano* **2015**, *9*, 5976.
[19] N. R. Pradhan, D. Rhodes, S. Feng, Y. Xin, S. Memaran, B.-H. Moon, H. Terrones, M. Terrones, L. Balicas, *ACS Nano* **2014**, *8*, 5911.
[20] M. Tosun, S. Chuang, H. Fang, A. B. Sachid, M. Hettick, Y. Lin, Y. Zeng, A. Javey, *ACS Nano* **2014**, *8*, 4948.
[21] A. Pospischil, M. M. Furchi, T. Mueller, *Nat. Nanotechnol.* **2014**, *9*, 257.
[22] Y. J. Zhang, J. T. Ye, Y. Yomogida, T. Takenobu, Y. Iwasa, *Nano Lett.* **2013**, *13*, 3023.
[23] S. Jo, N. Ubrig, H. Berger, A. B. Kuzmenko, A. F. Morpurgo, *Nano Lett.* **2014**, *14*, 2019.
[24] Y. Li, C.-Y. Xu, J.-Y. Wang, L. Zhen, *Sci. Rep.* **2014**, *4*, 7186.
[25] M.-L. Tsai, S.-H. Su, J.-K. Chang, D.-S. Tsai, C.-H. Chen, C.-I. Wu, L.-J. Li, L.-J. Chen, J.-H. He, *ACS Nano* **2014**, *8*, 8317.
[26] P. J. Jeon, S.-W. Min, J. S. Kim, S. R. A. Raza, K. Choi, H. S. Lee, Y. T. Lee, D. K. Hwang, H. J. Choi, S. Im, *J. Mater. Chem. C* **2015**, *3*, 2751.
[27] R. Cheng, D. Li, H. Zhou, C. Wang, A. Yin, S. Jiang, Y. Liu, Y. Chen, Y. Huang, X. Duan, *Nano Lett.* **2014**, *14*, 5590.
[28] T. Roy, M. Tosun, X. Cao, H. Fang, D.-H. Lien, P. Zhao, Y.-Z. Chen, Y.-L. Chueh, J. Guo, A. Javey, *ACS Nano* **2015**, *9*, 2071.
[29] M. M. Furchi, A. Pospischil, F. Libisch, J. Burgdörfer, T. Mueller, *Nano Lett.* **2014**, *14*, 4785.
[30] H. Fang, C. Battaglia, C. Carraro, S. Nemsak, B. Ozdol, J. S. Kang, H. A. Bechtel, S. B. Desai, F. Kronast, A. A. Unal, G. Conti, C. Conlon, G. K. Palsson, M. C. Martin, A. M. Minor, C. S. Fadley, E. Yablonovitch, R. Maboudian, A. Javey, *Proc. Natl. Acad. Sci. USA* **2014**, *111*, 6198.
[31] C.-H. Lee, G.-H. Lee, A. M. van Der Zande, W. Chen, Y. Li, M. Han, X. Cui, G. Arefe, C. Nuckolls, T. F. Heinz, J. Guo, J. Hone, P. Kim, *Nat. Nanotechnol.* **2014**, *9*, 676.
[32] Y. Deng, Z. Luo, N. J. Conrad, H. Liu, Y. Gong, S. Najmaei, P. M. Ajayan, J. Lou, X. Xu, P. D. Ye, *ACS Nano* **2014**, *8*, 8292.
[33] L. Zhou, K. Xu, A. Zubair, A. D. Liao, W. Fang, F. Ouyang, Y.-H. Lee, K. Ueno, R. Saito, T. Palacios, J. Kong, M. S. Dresselhaus, *J. Am. Chem. Soc.* **2015**, *137*, 11892.
[34] Y. H. Lee, X. Q. Zhang, W. Zhang, M. T. Chang, C. T. Lin, K. D. Chang, Y. C. Yu, J. T. W. Wang, C. S. Chang, L. J. Li, *Adv. Mater.* **2012**, *24*, 2320.
[35] L. Peng, L. Hu, X. Fang, *Adv. Funct. Mater.* **2014**, *24*, 2591.
[36] J. Kang, S. Tongay, J. Zhou, J. Li, J. Wu, *Appl. Phys. Lett.* **2013**, *102*, 012111.
[37] H. Li, Q. Zhang, C. C. R. Yap, B. K. Tay, T. H. T. Edwin, A. Olivier, D. Baillargeat, *Adv. Funct. Mater.* **2012**, *22*, 1385.
[38] K. Martin, Response of a typical photodiode vs. wavelength of the incident light, https://commons.wikimedia.org/wiki/File%3AResponse_silicon_photodiode.svg. (accessed: April **2009**).
[39] I.-S. Jeong, J. H. Kim, S. Im, *Appl. Phys. Lett.* **2003**, *83*, 2946.
[40] C. J. Brabec, A. Cravino, D. Meissner, N. S. Sariciftci, T. Fromherz, M. T. Rispens, L. Sanchez, J. C. Hummelen, *Adv. Funct. Mater.* **2001**, *11*, 374.
[41] Y. T. Lee, S. R. Ali Raza, P. J. Jeon, R. Ha, H.-J. Choi, S. Im, *Nanoscale* **2013**, *5*, 4181.